Generation of nondiffracting Bessel beam using digital micromirror device

Article *in* Applied Optics · June 2013

Impact Factor: 1.78 · DOI: 10.1364/AO.52.004566

8 authors, including:

Lei Gong
University of Science and Technology of Ch…
26 PUBLICATIONS **63** CITATIONS
SEE PROFILE

Yuxuan Ren
San Francisco State University
38 PUBLICATIONS **143** CITATIONS
SEE PROFILE

MIn-Cheng Zhong
University of Science and Technology of Ch…
20 PUBLICATIONS **120** CITATIONS
SEE PROFILE

Ziqiang Wang
University of Science and Technology of Ch…
23 PUBLICATIONS **146** CITATIONS
SEE PROFILE

Generation of nondiffracting Bessel beam using digital micromirror device

Lei Gong,[1] Yu-Xuan Ren,[2,3,5] Guo-Sheng Xue,[1] Qian-Chang Wang,[1] Jin-Hua Zhou,[1] Min-Cheng Zhong,[1] Zi-Qiang Wang,[1] and Yin-Mei Li[1,4,*]

[1]Department of Optics and Optical Engineering, University of Science and Technology of China, Hefei 230026, China

[2]National Center for Protein Sciences (Shanghai), Shanghai Institutes for Biological Sciences, CAS, Shanghai 201210, China

[3]Institute of Biochemistry and Cell Biology, Shanghai Institutes for Biological Sciences, CAS, Shanghai 200031, China

[4]Hefei National Laboratory For Physical Sciences at the Microscale, University of Science and Technology of China, Hefei 230026, China

[5]e-mail: yxren@ustc.edu.cn

*Corresponding author:liyinmei@ustc.edu.cn

Received 3 April 2013; revised 27 May 2013; accepted 28 May 2013; posted 30 May 2013 (Doc. ID 188246); published 26 June 2013

We experimentally demonstrated Bessel-like beams utilizing digital micromirror device (DMD). DMD with images imitating the equivalent axicon can shape the collimated Gaussian beam into Bessel beam. We reconstructed the 3D spatial field of the generated beam through a stack of measured cross-sectional images. The output beams have the profile of Bessel function after intensity modulation, and the beams extend at least 50 mm while the lateral dimension of the spot remains nearly invariant. Furthermore, the self-healing property has also been investigated, and all the experimental results agree well with simulated results numerically calculated through beam propagation method. Our observations demonstrate that the DMD offers a simple and efficient method to generate Bessel beams with distinct nondiffracting and self-reconstruction behaviors. The generated Bessel beams will potentially expand the applications to the optical manipulation and high-resolution fluorescence imaging owing to the unique nondiffracting property.

OCIS codes: (140.3300) Laser beam shaping; (230.6120) Spatial light modulators; (140.3295) Laser beam characterization; (230.4685) Optical microelectromechanical devices; (050.1380) Binary optics.

http://dx.doi.org/10.1364/AO.52.004566

1. Introduction

As a primary kind of nondiffracting beam, Bessel beams have caused immense concerns recently. Such beams have properties of nondiffraction over propagation distance and self-healing beyond an obstacle. Those significant properties have been exploited for many applications in various fields since the beam was first proposed by Durnin *et al.* [1]. For instance, Bessel beam plane illumination microscopy makes it possible to noninvasively image the three-dimensional cellular structures and to observe the rapid biological processes in individual living cells with a large penetration depth [2–4]. Bessel beam has also been involved in the field of optical micromanipulation and it is regarded as the tractor beam [5–10]. Optical micromanipulation and orientation of rod-like microspheres can be achieved with nondiffracting Bessel beam optical tweezers [5,7]. Especially, their ability of self-reconstruction has been fully exploited to enable microscopic particles manipulation in multiple planes simultaneously [7], and this provides a means to guide microscopic particles along the light propagation direction. In addition to the aforementioned applications, such beams have also been used in areas ranging from nonlinear optics [11–13], atom optics [14,15], and

1559-128X/13/194566-10$15.00/0

microfabrication [16] to optical communications [17], optical injection [18], and materials processing [19]. New applications of such beams are continuously explored as well as new generation and characterization methods. Among them, the zero-order Bessel beam is widely applied in many areas, such as high-resolution fluorescence imaging and optical micromanipulation and will be potentially applied in single molecule fluorescence detection [20,21].

Theoretical zero-order Bessel beam, whose lateral field profile is described in terms of zero-order Bessel function of the first kind, is of infinite energy; hence it cannot be effectively produced experimentally. However, over a finite range, approximate beams are realizable with intensity pattern independent of propagation distance [22]. There exist several experimental methods to obtain the desired beam profiles. Researchers originally employed an annular slit and a Fourier transform lens for the physical realization of Bessel beams [1,23,24]. Nevertheless, the aperture has a very low transmittance, so this restricts the transmission of laser power and is very inefficient for applications that require higher laser intensity. Afterwards, researchers developed methods utilizing axicons for the generation of Bessel beams. An axicon, either refractive or diffractive, may be the most common and convenient way to generate a Bessel beam. The approach based on refractive axicon is widely applied due to its high efficiency [25], but the parameters of the beam are fixed since the cone angle of a conventional axicon determines the spatial frequency of the beam. The problem is successfully addressed afterward by using a liquid-immersion axicon [22] or a fluid based tunable device [26], which allows the alteration of the axicon angle. In addition, other methods are also explored to obtain the desired optical pattern, including tunable acoustic gradient lens [27], $4-f$ spatial filtering system [28], computer generated holograms [29], magnetic liquid deformable mirror [30], and a pair of metal axicon mirrors [31]. Most recently, the liquid crystal spatial light modulator (SLM) enables online generation and direct projection of artificial phase pattern possible for beam shaping, therefore Bessel beams can be produced with a tunable phase pattern projected onto the pure phase SLM [32,33]. Although providing programmable generation of desired beams, relatively low damage thresholds of the common SLMs restricts their actual applicability. Moreover, recent progress of vector Bessel beam [15,34] and ultrashort Bessel beam pulse [35] will greatly promote their applications in various disciplines.

The digital micromirror device (DMD) is a microelectronic mechanical system. It was invented by Larry J. Hornbeck of Texas Instruments Inc. in 1987. DMD is an amplitude type SLM made up of aluminum mirror arrays and silicon based CMOS electronics. It has a relatively higher frame rate and damage thresholds compared with liquid crystal on silicon SLM. It has already been used in digital light processing [36,37] and will prospectively be employed for the next generation of digital displays. Meanwhile, emerging applications, such as holographic data storage, lithography, medical imaging, and 3D metrology are now available by using the reflected mirrors [38]. Recently, its advantages have been fully exploited to optically manipulate the spatiotemporal neuronal activity patterns of zebrafish [39]. Furthermore, the device also enables the programmable generation of novel light beams, such as Laguerre–Gaussian beams [40,41].

A DMD provides a promising option for obtaining Bessel beams. In the present work, we demonstrate a novel approach using DMD for generation of the zero-order Bessel beam with distinct nondiffracting property. Section 2 briefly reviews the analytical description of Bessel beam and the theory of beam propagation methods (BPMs) used for simulation of propagation behavior over distance, and theoretically describes the Bessel beam generation method with DMD. Section 3 introduces the experimental setup employed for shaping Bessel beam with DMD and the necessary procedure for utilization of DMD. Section 4 presents the transversal and longitudinal patterns of Bessel beams and experimentally demonstrates the nondiffracting and self-healing characteristics of the generated Bessel beam. Ideally DMD modulates the amplitude of the wavefront, thus the phase is simultaneously modulated due to the geometric structure of the device. Section 5 discusses the phase modulation in the experiment. The last section briefly summarizes the experimental generation and verification through propagation simulation of the Bessel beam.

2. Principle

In optical sciences, diffraction is the most common phenomena associated with the wave nature of light against propagation. This behavior of diffraction obeys the Maxwell wave equation. This equation, appropriate for free space, can be expressed as follows [42]:

$$\left(\nabla^2 - \frac{1}{c^2}\frac{\partial^2}{\partial t^2}\right)\psi(\rho,\phi,z,t) = 0. \tag{1}$$

There are a variety of solutions to this equation, and each of them corresponds to a kind of optical distribution as the theory of electromagnetism predicts. Furthermore, we can write the solution of integral form to Eq. (1) in terms of a monochromatic azimuthally symmetric wave $f(\rho)$. In terms of the light source at the plane $z = 0$, the corresponding equation is given in cylindrical coordinate system with the form [43]:

$$\psi(\rho,\phi,z,t) = \frac{k}{2\pi i}\iint \rho' \mathrm{d}\rho' \mathrm{d}\phi' f(\rho')\frac{e^{i(kR-\omega t)}}{R}, \tag{2}$$

where $k = 2\pi/\lambda$ is free-space wave vector of the electromagnetic field with frequency ω and

wavelength λ. $\rho = \sqrt{x^2 + y^2}$ denotes radial distance from the optical axis z, and R represents the distance from the light source to observation point (ρ, ϕ, z). When the condition of paraxial approximation is satisfied, we have

$$R = \sqrt{z^2 + \rho^2 + \rho'^2 - 2\rho\rho' \cos(\phi' - \phi)} \approx z + \frac{\rho^2 + \rho'^2 - 2\rho\rho' \cos(\phi' - \phi)}{2z}. \quad (3)$$

Under such condition, a special class of solutions with similar form can be obtained with complex amplitude of [44]

$$\psi_n(\rho, \phi, z) = A \exp(i(k_z z - \omega t)) J_n(k_\rho \rho) \exp(\mathrm{i}n\phi). \quad (4)$$

This solution exactly fulfills the scalar diffraction theory since the theory itself is approximate. In Eq. (4), $n = 0, \pm 1, \pm 2 \cdots$, $k_\rho = k \sin\theta$ and $k_z = k \cos\theta (k = (k_\rho^2 + k_z^2)^{1/2})$ are the radial and longitudinal wave vectors of light, respectively, while J_n stands for the nth-order Bessel function of the first kind. As a result, this series of optical distributions are named as Bessel beams with amplitude $A_n = AJ_n(k_\rho \rho)$ and the azimuthal phase $\exp(\mathrm{i}n\phi)$.

In this paper we focus on the generation of zero-order Bessel beam. The complex amplitude of the zero-order Bessel beam can be easily written through substituting 0 for n in Eq. (4), then

$$E(\rho, \phi, z) = A \exp(ik_z z) J_0(k_\rho \rho), \quad (5)$$

where the carrier with frequency ω is separated. Interestingly, the time-averaged intensity profile for Bessel beam remains invariant over the propagation distance in theory, as is revealed by the following expression [45]

$$I(\rho, \phi, z > 0) = I(\rho, \phi, z = 0) = \frac{1}{2} |\psi(\rho, \phi, z, t)|^2 \propto |J_0(k_\rho \rho)|^2. \quad (6)$$

This is an indication that as the beam propagates, it does not spread out, therefore, it is referred to the nondiffracting beam. Since the intensity profile is proportional to the square of zero-order Bessel function, the pattern of the ideal beam should be a set of concentric rings with a bright spot in the center.

According to the principle of interference, the superposition of monochromatic plane waves propagating on a cone will bring about a zero-order Bessel beam [1]. An axicon, or conical lens element, can transform the collimated beam into a set of plane waves propagating on a cone since the phase function depends linearly on the radius of the axicon [25]. So in order to generate the Bessel beam with DMD, first we need to calculate the pattern imitating the linear phase function of the axicon, in which the grayscale is linear to the radial distance as is shown in Fig. 1(d). Afterward, through loading the calculated image onto DMD, the Bessel beam will be produced though it is just an approximate due to the finite energy.

Since only an approximation to the ideal Bessel beam can be achieved experimentally, the optical distribution is not exactly described by Eq. (6). As for the optical profile of generated beam over propagation distance, the free-space BPM [46,47] is adopted to calculate the optical distribution. The wavefunction $\psi(x, y, z, t)$ comprises a complex amplitude $\psi_p(x, y, z)$ and a carrier with frequency ω, i.e., $\psi(x, y, z, t) = \mathrm{Re}\{\psi_p(x, y, z) \exp(i\omega t)\}$. The Helmholtz equation for $\psi_p(x, y, z)$ is

$$\frac{\partial^2 \psi_p}{\partial x^2} + \frac{\partial^2 \psi_p}{\partial y^2} + \frac{\partial^2 \psi_p}{\partial z^2} + k^2 \psi_p = 0, \quad (7)$$

where $k = \omega/c$ is wavenumber. Through Fourier transform of Eq. (7), we obtain

$$\frac{d^2 \Psi_p}{dz^2} + k^2 \left(1 - \frac{k_x^2}{k^2} - \frac{k_y^2}{k^2}\right) \Psi_p = 0, \quad (8)$$

where $\Psi_p(k_x, k_y, z)$ is the 2D Fourier transform of $\psi_p(x, y, z)$, and it can be numerical reconstructed through

$$\Psi_p(k_x, k_y, z) = \Psi_{p0}(k_x, k_y) \exp\left(-ikz\sqrt{1 - \frac{k_x^2}{k^2} - \frac{k_y^2}{k^2}}\right), \quad (9)$$

where $\Psi_{p0}(k_x, k_y)$ is the light distribution in the frequency domain at $z = 0$. Through inverse Fourier transform, $\psi_p(x, y, z)$ can be generated from Eq. (9). So Eq. (9) provides a means to relate the intensity distribution of light at two arbitrary planes separated with distance z along the propagation direction. BPM algorithm is achieved by repeating the algorithm Eq. (9) to reconstruct the light intensity along z direction step by step. In this work, BPM method is employed to numerically calculate the intensity distribution in x–z plane for ideal Bessel beam and obstructed Bessel beam.

3. Experimental Setup

We take advantage of a commercial DMD [0.7 in. (1.78 cm), XGA] manufactured by Texas Instruments Inc. in the experiment. The device, which consists of a matrix of 1024 × 768 micromirrors deposited on silicon chip with a 14.46 μm pixel pitch, is mounted onto an underlying circuit board controlled by a custom computer. The square mirror is 13.68 μm width on each side and those tiny mirrors are coated with aluminum to achieve maximum reflectivity. For making full use of incident light, the interval between two

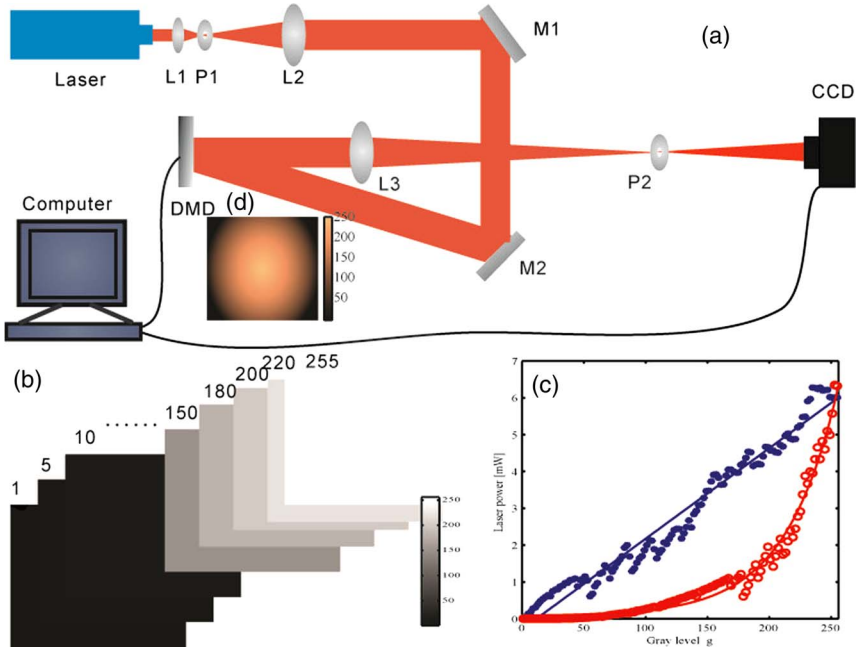

Fig. 1. Experiment layout and gamma curve correction of DMD. (a) Schematic of the experimental setup. The laser utilized is a He–Ne laser with wavelength 632.8 nm. A telescope ($f_1 = 30$ mm, $f_2 = 150$ mm) is employed to expand the beam to 10 mm in diameter. In order to improve the beam quality, a pinhole P1 with diameter 500 μm is adopted to filter the laser beam. The expanded and collimated laser beam is then steered to uniformly illuminate the surface of DMD with precise incident angle of 24° through adjustment of mirrors M1, M2. The DMD modulates the laser profile through projection of gray scale holograms and the incident Gaussian beam was transformed to Bessel beam through intensity modulation exerted by DMD. Then convex lens L3 ($f = 250$ mm) is employed to collect the modulated light. A pinhole P2 placed near the back focal plane of the lens selectively passes the first diffraction order of beam. The optical intensity profile is digitalized and recorded by a CCD camera (MINTRON MTV-1881EX 795 × 596) mounted on a guide rail for multiplane image collection. When performing the energy measurements, the camera is replaced by a power meter (Thorlabs, PM100D). (b) Image sequence with gray value from 0 to 255 used to test the intensity response property of DMD. The gray scale changes gradually from black to white when increasing the gray level. (c) Experimental results of the measured gamma response: uncorrected gamma curve (red hollow dots) and corrected gamma curve (blue solid dots). (d) The corrected image used to generate the Bessel beam. The desired beam is formed behind the mirrors irradiated by an expanded Gaussian beam as long as the corrected image is projected onto the DMD.

mirrors is fabricated to be approximately 0.78 μm so that the mirrors have an excellent fill factor of about 89.5%. The optical element can be taken as the ordinary mirror when the device is powered off. While it is turned on, according to status of the dual memory cell that stores "1" or "0", each mirror can move to +12 or −12 deg in terms of the main diagonal line. These two kinds of angular positions correspond to an "on" and "off" state, which stand for reflecting the beam toward the rear optical system and sending the output beam to a light absorber, respectively. That means each mirror of DMD addressed individually serves as a light switch. The main function of the device is to modulate the amplitude of an incident beam. In principle, this is realized by regulating the duty ratio, actually via binary pulse width modulation, which can be controlled by the computer using custom software. We can easily acquire the desired optical profile at imaging plane so long as the same pattern is loaded on the DMD.

Experimental arrangement of the Bessel beam generation using a DMD is illustrated in Fig. 1(a). A He–Ne laser at the wavelength $\lambda = 633$ nm that emits Gaussian mode beam (beam waist $\omega_0 = 1$ mm) with power about 13 mW serves as the light source. A pinhole P1 with diameter 500 μm is utilized to improve the beam quality. Lens L1 ($f = 30$ mm) and Lens L2 ($f = 150$ mm) constitute a telescope, and this telescope expands the laser beam by five times to approximately 10 mm in diameter. Two mirrors M1 and M2 are employed to steer the collimated laser beam to uniformly illuminate its surface with precise incident angle of 24° with respect to the normal direction of the DMD surface. DMD modulates the amplitude of the incident beam by means of loading a precalculated intensity pattern onto it. Consequently, the Bessel beam is generated behind the DMD along the optical axis. A lens L3 ($f = 250$ mm) is exactly placed at the position focal distance away from the DMD to collect the reflected light. In order to obtain the desired optical pattern, the first-order diffraction is picked up by a tunable pinhole P2 placed near the back focal plane of the lens L3, which prevents other orders of diffraction including the zero-order of diffraction from entering the detector. The detector employed to record the far field images of beam profile is a charge-coupled device (CCD) (Mintron MTV-1881EX, Shenzhen, China, pixel size 6.5 μm width, 795 pixels × 596 pixels), which at first is placed about 10 mm after the pinhole P2. The CCD is mounted on a movable guide rail to collect

a series of cross-sectional distributions of the light field. 3D distribution of the light field can be reconstructed from the cross-sectional measurements. In the experiment, the power of the produced beams is attenuated by neutral density filters (Thorlabs, America) to avoid gain saturation of the CCD camera. By replacing the CCD with a power meter (Thorlabs, PM100D, S140c detector, America), we were able to measure the laser intensity near the focal plane of Lens L3.

Usually, the relationship between output signal and input signal for display devices are not linear, such as liquid crystal display, as does DMD. In order to improve the beam quality, the optical system should work in the linear range. First, we experimentally test the intensity response of the reflected beam to the gray value of projected image, which is defined as the gamma curve of the device. The experiments are conducted by successively projecting images with uniform gray scale from 0 to 255 (Fig. 1(b)) on the DMD, and measuring the power of the output beam. As a consequence, the measured gamma curve is not linear as illustrated in the red curve of Fig. 1(c). Therefore, we adopt image correction method described in [40] to correct the gamma curve. The intensity response property is enhanced by means of a correction function calculated from the previously measured data, resulting in a linear response. With the corrected function, we generate a corrected image sequence with uniform gray value from 0 to 255 and repeat the same measurements with corrected image sequence. As is shown in blue solid dots of Fig. 1(c), the measured gamma curve is linear after correction. As expected, the optical setup functions well now, and upon that condition we utilize it to produce Bessel beams.

As for the verification of nondiffraction property of the beam, we measure the intensity profile of the beam in transverse planes at an interval of 1 mm along the z axis, and subsequently reconstruct the spatial intensity distribution of the reflected beam for further comparison with theoretically simulated results.

4. Results

A. Bessel Beam Generation

As Durnin revealed, an ideal Bessel beam can be formed by means of a linear superposition of monochromatic plane waves propagating on a cone [1]. For transformation of a Gaussian laser beam into a Bessel beam, we calculate the images imitating the equivalent axicon, in which the grayscale is linear to the radial distance, while the images are not perfect due to the nonlinear gamma response. Taking into account of the gamma curve correction, we enhance the precalculated images to enable the desired beam generation. Through loading the corrected image (Fig. 1(d)) onto DMD, the Bessel-like beam is formed in the far field behind the mirrors irradiated by an expanded Gaussian beam. Afterward, one can easily observe the optical distributions at different distance using a CCD camera translated along the z axis. As is illustrated in Fig. 2, a typical cross-sectional image of the generated field, which is recorded at a distance of $z = 30$ mm from the back focal plane of the convex lens L3 (Fig. 1(a)), displays a pattern comprised of ring systems with a bright central core. Then the one-dimensional transverse intensity profiles of the beams can be reconstructed from the CCD images. Corresponding graphs in Fig. 2 are measured transverse intensity profile (blue line) and theoretically calculated Bessel beam profile (red line) in a horizontal (right) and vertical (bottom) section, respectively. The fitting function is with the form of

$$I(\rho) = AJ_0^2(k_\rho(\rho - \rho_0)) + B, \tag{10}$$

where A, B, k_ρ, ρ_0 are fitting parameters obtained from the measured data. The center of the laser spot is set as the origin of the coordinate, therefore, through fitting of the gray scale along the horizontal dashed line with Eq. (10), the parameters can be determined as $A = 200$(a.u.), $B = 40$(a.u.), $\rho_0 = 0$, $k_\rho = 40$/mm. Generally, the experimental beam profiles show an agreement with the simulation, although there is some distortion on the measurement mainly because of the innate phase modulation of the DMD. This is a direct indication that the Bessel-like beam has been successfully generated using DMD.

As mentioned above, an ideal Bessel beam is taken as a superposition of a set of plane waves propagating on a cone. Likewise, the Bessel beam can be decomposed into plane waves with wave vectors lying on the surface of a cone, and its Fourier transform is a ring in spatial frequency domain. While half of the vertex angle of the cone can be derived from the decomposition to provide a method to characterize the Bessel beam [44]. The angle of the form

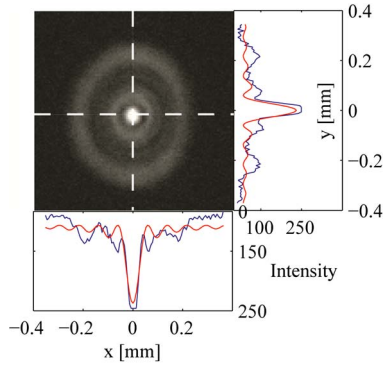

Fig. 2. Representative cross-sectional image of generated Bessel beam at a distance of $z = 30$ mm from the back focal plane of the convex lens (L3, Fig. 1) behind the DMD. Accompanying graphs are radial intensity profiles (blue line) fitted to zero-order Bessel function squared (red line) at x (bottom) and y (right) axis, respectively. The measured intensity distribution is in accordance with theoretical predictions.

$\theta = \sin^{-1} k_\rho/k$, where k and k_ρ are the wave vector and its transverse component, is employed to characterize the divergence of the generated Bessel beam. According to the properties of the zeros of the Bessel function, we can obtain [30]

$$\theta \approx \frac{2.405\lambda}{2\pi r_0}, \tag{11}$$

where r_0 is the first zero of the transverse intensity profile of the produced beam and λ is wavelength. In our experiment of Bessel beam generation, $r_0 \approx 60$ μm is derived from the measured intensity profile corresponding to the cross-sectional image in Fig. 2. That means, the generated Bessel beam has an angle of about 4 mrad.

B. Diffraction-free Behavior of the Generated Bessel Beam

One of the major properties for Bessel beam is nondiffraction. To verify this property, a series of cross-sectional images were collected by a CCD camera near the back focal plane of the projection lens and the distance between each consecutive image was 1 mm along the light propagation direction. Further, the pixel values for one central line was taken from each image and all the lines were reconstructed by a custom computer program to reconstruct the intensity distribution for Bessel beam in the x–z plane (Fig. 3(b)). As a comparison, theoretical intensity distribution along x–z plane can be numerically simulated through BPM algorithm (Fig. 3(a)). The experimentally created Bessel beam was well verified via the comparison with theoretical distribution. In addition, the 3D view of the optical field derived from the stack of images is also shown in Fig. 3(e), which manifests that we have experimentally reconstructed the spatial optical field of the generated beam. All the observed results demonstrate that the structure of the produced pattern remains stable along with the beam propagation, and this is a direct indication of the nondiffracting characteristics of the Bessel beams.

Furthermore, in order to quantitatively characterize the nondiffracting property of the generated beams, we employ full width at half-maximum (FWHM) [31] of the central spot to characterize the size of the beam, while it can be used to display the changes of the central spot more intuitively. In order to observe the behavior of the central spot, we first obtain the FWHM spot size at a certain propagation distance by numerically fitting the measured transverse intensity profile with zero-order Bessel function. In theory, the value of FWHM is $2.252/k_\rho$ derived from Eq. (10) for a zero-order Bessel beam. Then the spot size can be obtained by substituting the parameter k_ρ with fitting result, for instance, 60 μm (FWHM along x axis) corresponding to the profile in Fig. 3(c). Theoretically, the dimension of the central spot keeps constant for the ideal Bessel beams, while the spot size is variable along with the beam propagation experimentally. According to

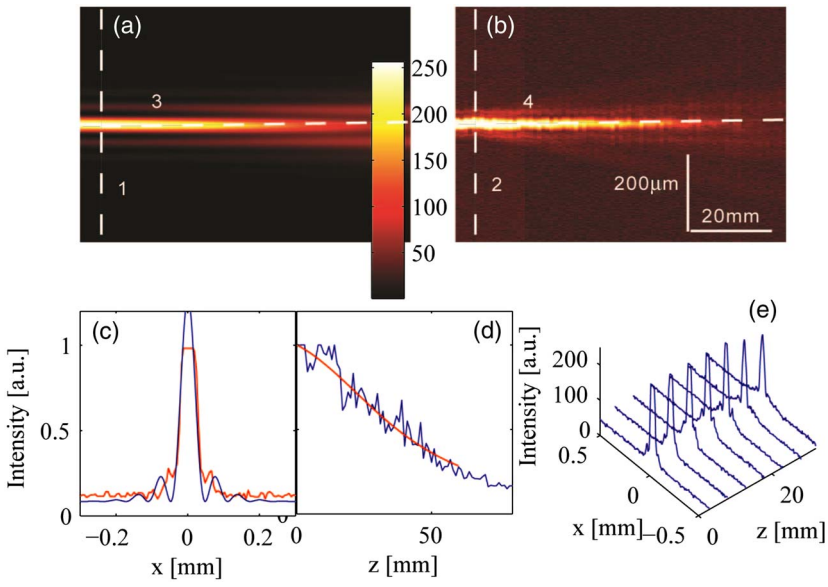

Fig. 3. Simulation and experimental results for nondiffraction behavior of Bessel beam. (a) Simulation results of optical intensity profile at x–z plane. A free-space BPM is adopted to calculate the spatial optical intensity distribution. (b) Experimental results of optical intensity profile at x–z plane, which demonstrates the intensity evolution of the generated beam along with propagation. (c) The transverse intensity profile (blue) of the generated beam at 25 mm (Line 2) and its fitting curve (red). The FWHM ($2.252/k_\rho$) obtained from the fitting result is 60 μm, and the range of nondiffraction can be derived from measurement to be about 50 mm. (d) The normalized on-axis (Line 4) intensity versus propagation distance of the generated Bessel beam (blue curve) and the simulation on-axis (Line 3) intensity (red curve) corresponding to Line 3. (e) 3D plots of the optical distribution of a generated Bessel beam through analysis of the cross-sectional images. The cross-sectional images are captured at an interval of 1 mm by translating the CCD camera from back focal plane of the projection lens along the beam path.

the above method, the FWHM for different propagation distance is obtained and further measurement reveals that the Bessel-like beam extends at least 50 mm along optical axis while the transverse dimension of the central spot nearly remains invariant. Compared with a Gaussian beam with equivalent spot size, it is much longer than the Rayleigh range $Z_R = (\pi\omega_0^2/\lambda) \approx 17.8$ mm of the Gaussian beam. Moreover, the normalized on-axis intensity versus propagation distance of the resulting beam is also investigated as illustrated in Fig. 3(d). Corresponding to central intensity of a Gaussian beam at Rayleigh range (quarter of the maxima), the intensity value appears at about 50 mm for the generated beam. The experimental data proves that we have generated a Bessel-like beam with a very large axial distance, which is useful for super-resolution microscopy and optical manipulation deep inside the live biological sample.

C. Self-Healing Property

In principle, even obstructed, the transverse intensity distribution of the Bessel light beam will be reconstructed behind the obstacle owing to the remarkable ability of self-healing [48]. In order to experimentally testify this unique behavior, we utilize a glass slide with an ink dot, whose diameter is about 400 microns, as an obstacle placed directly in the beam path to block the central portion of the beam, and observe the self-healing effect by reconstruction of 3D spatial distribution of the field in presence of the perturbation. Likewise, a series of cross-sectional images are captured at an interval of 1 mm within a range of 60 mm using a CCD camera, then the spatial intensity distribution of the optical field after disturbance is investigated. As is illustrated in Fig. 4(b), intensity distribution in x–z plane is shown as the beam propagates behind the obstruction. The intensity of the central portion increases gradually behind the obstacle until the bright central spot appears and remains its intensity for a long distance, revealing the self-reconstruction ability of the generated beam. To compare the measured results with the theoretical predictions, we adopt the BPM algorithm to simulate the propagation of the light electric field behind the obstruction, and the simulation result is shown in Fig. 4(a), and the simulation shows a good agreement with the measured results.

Further, in order to verify that the reconstructed beam is a Bessel beam, we investigated the transverse profiles of distorted beam in detail. First the transverse profile (blue curve) at the focal plane just behind the obstacle is shown in Fig. 4(c) together with the simulation result (red curve), indicating that the central part of the Bessel beam is obstructed. Then we observed the behavior of the distorted beam along the propagation direction at several certain distances. The experimental intensity profiles (blue curve) at 14 and 33 mm behind the obstruction are shown in Figs. 4(d) and 4(e), and the red and purple curves are simulation and fitting results, respectively. Direct comparison

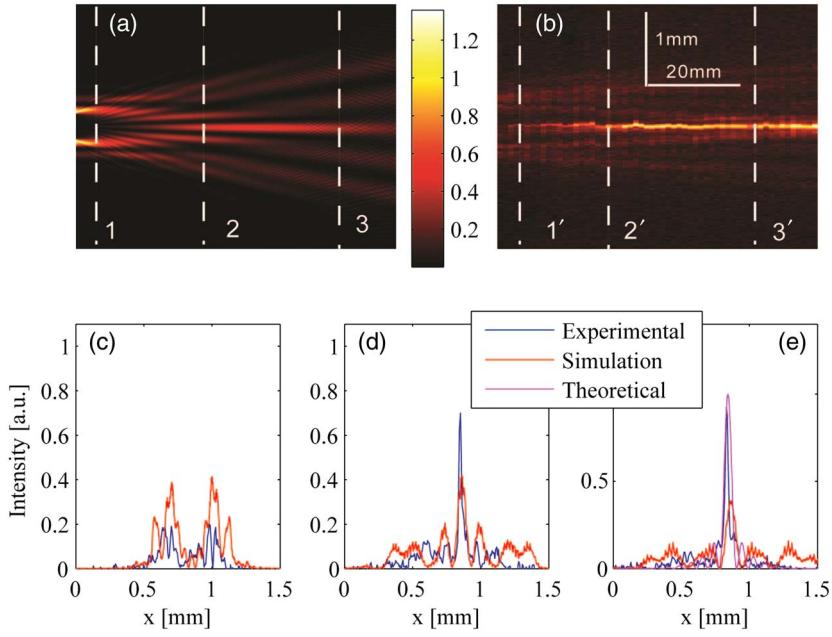

Fig. 4. Self-healing results of the generated Bessel beam. (a) Simulated intensity distribution of the obstructed beam at x–z plane. The sizes of the Bessel beam and the circular opaque obstacle are about 700 and 400 μm, respectively. (b) Experimental intensity profile of the Bessel beam at x–z plane in presence of an obstacle. An ink dot fixed on a glass slide with diameter of about 400 microns is used as an opaque obstacle placed directly in the beam path to block the central portion of the beam. (c) The simulated (red curve) and measured (blue curve) transverse intensity profile of the obstructed beam just behind the obstacle in the focal plane (1 and 1′). The central portion is obstructed, which can be seen from the plot. (d) The measured (blue) and simulated (red) transverse intensity profiles of the obstructed beam at 14 mm (2 and 2′) behind the obstacle. (e) The transverse intensity profile (blue) of the obstructed beam at 33 mm behind the obstacle, accompanying with the simulating (red) and theoretical (purple) curves (3 and 3′).

shows that the transverse profile at 14 mm agrees with the simulation, but is not as good as the profile of a Bessel Beam, because the distorted beam is in the process of self-healing. While the experimental transverse profile at 33 mm agrees with simulation, indicating that the distorted beam has self-constructed to be a Bessel beam. All the experiments demonstrate that the Bessel-like beam with self-healing property can be generated with DMD.

5. Discussions

As mentioned in the subsection of Bessel beam generation, the produced Bessel mode beams have some distortion compared with theoretical ones. There are many reasons resulting in this phenomenon, such as the angle deviation of incident beam relative to DMD, the quality of the calculated images, the mode quality of coherent light, disturbance of the stray light, phase modulation of DMD. Among them, the phase modulation of DMD and the angle deviation of incident beam are the dominant factors in our experiment. In the following, we will briefly discuss these influence factors.

The DMD has inherent phase modulation though we regard the device as an amplitude-only SLM. Phase modulation of the incident beam by DMD is so complex that we consider a simple situation where all mirrors are in the "on" state. Then a DMD is actually an analogue of two-dimensional diffraction grating [49], illustrated in Fig. 5. First we introduce the concept of main-diagonal and side-diagonal, corresponding to rotation direction of the mirrors (magenta dashed line) and its perpendicular direction (blue dashed line). The mirrors along the main-diagonal remain in the same plane after rotation, while those along the side-diagonal are in different planes. Therefore, mirrors along the line parallel to the main-diagonal are modeled as an one-dimensional mirror array, and those along the line parallel to the side-diagonal can be taken as a blazed grating structure with blazing angle of φ (rotation angle, depicted in the bottom of Fig. 5), and these two gratings have the same constant of $\sqrt{2}d_0/2$ (d_0 is the mirror spacing). As a consequence, the incident beam is subjected to complex phase modulation exerted by DMD. According to Fraunhofer diffraction, the intensity of diffraction field after modulation with all mirrors on can be calculated with the form of [50]

$$I = A_0^2 d_0^4 \frac{\sin^2[(2M)u']}{\sin^2 u'} \frac{\sin^2[(2N)u'']}{\sin^2 u''} \times \mathrm{sinc}^2(\nu') \cdot \mathrm{sinc}^2(\nu''), \tag{12}$$

where

$$u' = \frac{\pi d_0}{\lambda}(\sin\theta\cos\phi - \sin\theta_0\cos\phi_0), \tag{13a}$$

$$u'' = \frac{\pi d_0}{\lambda}(\sin\theta\sin\phi - \sin\theta_0\sin\phi_0), \tag{13b}$$

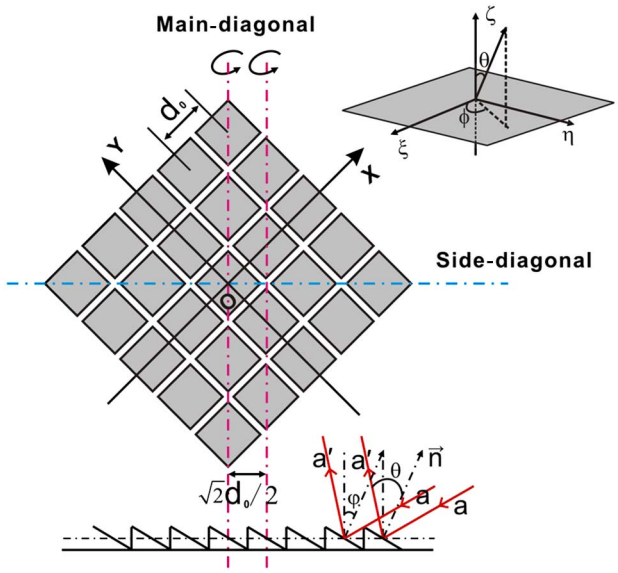

Fig. 5. Schematic diagram of DMD modeled as a 2D diffraction grating. Coordinate system (x, y, z) with the origin at the center of the rectangular DMD is established for calculation of diffraction field. $(2M + 1) \times (2N + 1)$ square mirrors with mirror spacing d_0 is considered to form the device, and each mirror is encoded by the location of its center. Each mirror addressed individually can tilt either +12 deg ("on") or −12 deg ("off") along the main-diagonal (magenta dashed line). With all mirrors on, mirrors along the lines parallel to the main-diagonal are taken as a one-dimensional plane mirror array, while those along the lines parallel to the side-diagonal (blue dashed line) are modeled as a blazed grating with constant of $\sqrt{2}d_0/2$ and blazed angle of $\varphi = 12°$, depicted at the bottom of the figure. The red lines stand for incident ray and diffraction ray, and the diffraction angle is θ. Top right graph demonstrates a local coordinate system (ξ, η, ς) introduced in the m-n-th mirror, which can be transferred into a spherical coordinate (r, θ, ϕ).

$$\nu' = \frac{\pi d_0}{\lambda}\left[(\sin\theta\cos\phi - \sin\theta_0\cos\phi_0) + \frac{\tan\varphi}{\sqrt{2}}(\cos\theta - \cos\theta_0)\right], \tag{13c}$$

$$\nu'' = \frac{\pi d_0}{\lambda}\left[(\sin\theta\sin\phi - \sin\theta_0\sin\phi_0) + \frac{\tan\varphi}{\sqrt{2}}(\cos\theta - \cos\theta_0)\right]. \tag{13d}$$

(θ_0, ϕ_0) and (θ, ϕ) are the angles between incident ray and diffraction ray with respect to ς and ξ axis, respectively. (ξ, η, ς) is a local coordinate system established on the m-n-th mirror, illustrated at the top right corner of Fig. 5. The expression indicates the intensity distribution indeed has the similar form with the diffraction field of a two-dimensional diffraction grating. Optical distribution is not uniform behind the DMD and the diffraction energy tends to be concentrated due to the modulation of

sinc functions. Moreover, in our experiment not all the mirrors are in "on" state, which means that more complicated phase modulation is involved. This will influence the precision of intensity modulation and will consequently distort the wave front of generated Bessel beam.

In addition, the angle between the incident beam and the normal of DMD has a great impact on the beam generation. The diffraction of DMD can be analyzed using two-dimensional blazed grating theory, so the Fourier transform pattern of the two-dimensional array surface determines the envelope of diffraction [51]. The locations of envelope depend on the wavelength, the pixel pitch of micromirror and the incident angle. In our experiment, the wavelength and the grating pitch are fixed. Therefore, the incident angle influences the intensity distribution in beam generation. With adjustment of incident angle, the phase difference of optical rays reflected from neighboring mirrors varies, which results in the change of diffraction energy distribution. That means the optical field will be subjected to unexpected phase modulation.

Although the DMD has undesired phase modulation and the micromirror is subjected to angular fluctuation, it has been utilized to successfully generate Laguerre–Gaussian beam [40,41], and our experimental achievement of zero-order Bessel beams is another evidence that this device can convert the Gaussian mode into those modes with novel characteristics. It is worth to mention that the produced Bessel-like beams in our experiment demonstrate obvious properties of nondiffraction and self-reconstruction, which is most important for actual applications. Furthermore, we believe that our work also provides a potential way for generation of other complicated beam structures, such as Bessel beams with arbitrary trajectories [52] and cylindrical vector beams [53].

6. Conclusion

To summarize, we have proposed a simple and efficient approach for zero-order Bessel light beam generation using a commercial DMD. In the experiment, the collimated Gaussian beam is transformed into a Bessel-like beam through the DMD projected with a corrected axicon-like pattern. The output beam has the zero-order Bessel function profile in the far field, and the divergence of the generated Bessel beam is characterized to be 4 mrad. In addition, we experimentally reconstructed the 3D spatial optical field of the generated beam from a stack of cross-sectional images. On this basis, the nondiffracting and self-healing behaviors were investigated to further verify the beam characteristics. We analyzed the central spot intensity and FWHM for different propagation distances, and the results show that the generated beam can extend at least 50 mm while the lateral dimension (FWHM) of the spot remains about 60 μm, much longer than the Rayleigh range of a Gaussian beam of the same size. Moreover, obvious self-healing behavior was observed when an opaque slide with pattern was placed directly in the beam path to partially distort the produced beam. All the experimental results show a good agreement with theoretical predictions numerically calculated through the BPM method. Although there is some distortion between the produced beams and theoretical ones due to the innate phase modulation of the DMD, the generated quasi-Bessel beams demonstrate distinct behaviors of nondiffracting and self-healing, which will enable extensive applications in optical trapping, *In vivo* imaging, nonlinear optics, and materials processing.

L. G. and Y. R. contributed equally to this work. Y. R. acknowledges Dr. Y.-J. Yang at the University of Electronic Science and Technology of China for insightful discussions on theoretical analysis. This work was supported by the National Natural Science Foundation of China (Grant Nos. 21073174, 11204004, 31071064).

References

1. J. Durnin, J. Miceli, Jr., and J. Eberly, "Diffraction-free beams," Phys. Rev. Lett. **58**, 1499–1501 (1987).
2. T. A. Planchon, L. Gao, D. E. Milkie, M. W. Davidson, J. A. Galbraith, C. G. Galbraith, and E. Betzig, "Rapid three-dimensional isotropic imaging of living cells using Bessel beam plane illumination," Nat. Methods **8**, 417–423 (2011).
3. L. Gao, L. Shao, C. D. Higgins, J. S. Poulton, M. Peifer, M. W. Davidson, X. Wu, B. Goldstein, and E. Betzig, "Noninvasive imaging beyond the diffraction limit of 3D dynamics in thickly fluorescent specimens," Cell **151**, 1370–1385 (2012).
4. S. B. Purnapatra, S. Bera, and P. P. Mondal, "Spatial filter based Bessel-like beam for improved penetration depth imaging in fluorescence microscopy," Sci. Rep. **2**, 692 (2012).
5. J. Arlt, V. Garces-Chavez, W. Sibbett, and K. Dholakia, "Optical micromanipulation using a Bessel light beam," Opt. Commun. **197**, 239–245 (2001).
6. D. G. Grier, "A revolution in optical manipulation," Nature **424**, 810–816 (2003).
7. V. Garcés-Chávez, D. McGloin, H. Melville, W. Sibbett, and K. Dholakia, "Simultaneous micromanipulation in multiple planes using a self-reconstructing light beam," Nature **419**, 145–147 (2002).
8. V. Garcés-Chávez, D. Roskey, M. Summers, H. Melville, D. McGloin, E. Wright, and K. Dholakia, "Optical levitation in a Bessel light beam," Appl. Phys. Lett. **85**, 4001–4003 (2004).
9. D. B. Ruffner and D. G. Grier, "Optical conveyors: a class of active tractor beams," Phys. Rev. Lett. **109**, 163903 (2012).
10. D. McGloin, V. Garcés-Chávez, and K. Dholakia, "Interfering Bessel beams for optical micromanipulation," Opt. Lett. **28**, 657–659 (2003).
11. J. Arlt, K. Dholakia, L. Allen, and M. Padgett, "Efficiency of second-harmonic generation with Bessel beams," Phys. Rev. A **60**, 2438–2441 (1999).
12. P. Polesana, A. Dubietis, M. Porras, E. Kučinskas, D. Faccio, A. Couairon, and P. Di Trapani, "Near-field dynamics of ultrashort pulsed Bessel beams in media with Kerr nonlinearity," Phys. Rev. E **73**, 056612 (2006).
13. P. Polynkin, M. Kolesik, A. Roberts, D. Faccio, P. di Trapani, and J. Moloney, "Generation of extended plasma channels in air using femtosecond Bessel beams," Opt. Express **16**, 15733–15740 (2008).
14. B. Paredes, A. Widera, V. Murg, O. Mandel, S. Fölling, I. Cirac, G. V. Shlyapnikov, T. W. Hänsch, and I. Bloch, "Tonks–Girardeau gas of ultracold atoms in an optical lattice," Nature **429**, 277–281 (2004).

15. H. Wang, L. Shi, B. Lukyanchuk, C. Sheppard, and C. T. Chong, "Creation of a needle of longitudinally polarized light in vacuum using binary optics," Nat. Photonics **2**, 501–505 (2008).
16. X. F. Li, R. Winfield, S. O'Brien, and G. Crean, "Application of Bessel beams to 2D microfabrication," Appl. Surf. Sci. **255**, 5146–5149 (2009).
17. V. Kollarova, T. Medrik, R. Celechovsky, Z. Bouchal, O. Wilfert, and Z. Kolka, "Application of nondiffracting beams to wireless optical communications," Proc. SPIE **6736**, 67361C (2007).
18. H. A. Rendall, R. F. Marchington, B. B. Praveen, G. Bergmann, Y. Arita, A. Heisterkamp, F. J. Gunn-Moore, and K. Dholakia, "High-throughput optical injection of mammalian cells using a Bessel light beam," Lab Chip **12**, 4816–4820 (2012).
19. M. Duocastella and C. B. Arnold, "Bessel and annular beams for materials processing," Laser Photon. Rev. **6**, 607–621 (2012).
20. M. J. Comstock, T. Ha, and Y. R. Chemla, "Ultrahigh-resolution optical trap with single-fluorophore sensitivity," Nature Methods **8**, 335–340 (2011).
21. G. Sirinakis, Y. Ren, Y. Gao, Z. Xi, and Y. Zhang, "Combined versatile high-resolution optical tweezers and single-molecule fluorescence microscopy," Rev. Sci. Instrum. **83**, 093708 (2012).
22. S. Akturk, C. L. Arnold, B. Prade, and A. Mysyrowicz, "Generation of high quality tunable Bessel beams using a liquid-immersion axicon," Opt. Commun. **282**, 3206–3209 (2009).
23. T. Čižmár and K. Dholakia, "Tunable Bessel light modes: engineering the axial propagation," Optics Express **17**, 15558–15570 (2009).
24. M. A. Mahmoud, M. Y. Shalaby, and D. Khalil, "Propagation of Bessel beams generated using finite-width Durnin ring," Appl. Opt. **52**, 256–263 (2013).
25. G. Scott and N. McArdle, "Efficient generation of nearly diffraction-free beams using an axicon," Opt. Eng. **31**, 2640–2643 (1992).
26. G. Milne, G. D. M. Jeffries, and D. T. Chiu, "Tunable generation of Bessel beams with a fluidic axicon," Appl. Phys. Lett. **92**, 261101 (2008).
27. T. Tsai, E. McLeod, and C. B. Arnold, "Generating Bessel beams with a tunable acoustic gradient index of refraction lens," Proc. SPIE **6326**, 63261F (2006).
28. J. M. D. Kowalczyk, S. N. Smith, and E. B. Szarmes, "Generation of Bessel beams using a 4-*f* spatial filtering system," Am. J. Phys. **77**, 229–236 (2009).
29. J. H. Lee, S. J. Lee, C. S. Kyong, J. B. Song, Y. W. Lee, and C. H. Kwak, "Propagation characteristics of Bessel beam using phase type CGH," Proc. SPIE **4924**, 302–310 (2002).
30. D. Brousseau, J. Drapeau, M. Piché, and E. F. Borra, "Generation of Bessel beams using a magnetic liquid deformable mirror," Appl. Opt. **50**, 4005–4010 (2011).
31. S. K. Tiwari, S. R. Mishra, S. P. Ram, and H. S. Rawat, "Generation of a Bessel beam of variable spot size," Appl. Opt. **51**, 3718–3725 (2012).
32. R. Bowman, N. Muller, X. Zambrana-Puyalto, O. Jedrkiewicz, P. di Trapani, and M. Padgett, "Efficient generation of Bessel beam arrays by means of an SLM," Eur. Phys. J. Special Topics **199**, 159–166 (2011).
33. F. Courvoisier, P. A. Lacourt, M. Jacquot, M. Bhuyan, L. Furfaro, and J. Dudley, "Surface nanoprocessing with nondiffracting femtosecond Bessel beams," Opt. Lett. **34**, 3163–3165 (2009).
34. A. V. Novitsky and D. V. Novitsky, "Negative propagation of vector Bessel beams," J. Opt. Soc. Am. A **24**, 2844–2849 (2007).
35. F. Courvoisier, M. Jacquot, P. A. Lacourt, M. Bhuyan, L. Furfaro, R. Ferrière, and J. Dudley, "Generation of ultrafast Bessel micro-beams and applications to laser surface nanoprocessing," Proc. SPIE **7728**, 77281W (2010).
36. J. Liang, S. Y. Wu, R. N. Kohn, Jr., M. F. Becker, and D. J. Heinzen, "Bandwidth-limited laser image projection using a DMD-based beam shaper," Proc. SPIE **8254**, 82540M (2012).
37. J. M. Younse, "Projection display systems based on the digital micromirror device (DMD)," in *Micromachining and Microfabrication* (International Society for Optics and Photonics, 1995), pp. 64–75.
38. D. Dudley, W. Duncan, and J. Slaughter, "Emerging digital micromirror device (DMD) applications," Proc. SPIE **4985**, 14 (2003).
39. P. Zhu, O. Fajardo, J. Shum, Y. P. Z. Schärer, and R. W. Friedrich, "High-resolution optical control of spatiotemporal neuronal activity patterns in zebrafish using a digital micromirror device," Nat. Protoc. **7**, 1410–1425 (2012).
40. Y. X. Ren, M. Li, K. Huang, J. G. Wu, H. F. Gao, Z. Q. Wang, and Y. M. Li, "Experimental generation of Laguerre–Gaussian beam using digital micromirror device," Appl. Opt. **49**, 1838–1844 (2010).
41. V. Lerner, D. Shwa, Y. Drori, and N. Katz, "Shaping Laguerre–Gaussian laser modes with binary gratings using a digital micromirror device," Opt. Lett. **37**, 4826–4828 (2012).
42. J. Durnin, "Exact solutions for nondiffracting beams. I. The scalar theory," J. Opt. Soc. Am. A **4**, 651–654 (1987).
43. P. L. Overfelt and C. S. Kenney, "Comparison of the propagation characteristics of Bessel, Bessel–Gauss, and Gaussian beams diffracted by a circular aperture," J. Opt. Soc. Am. A **8**, 732–745 (1991).
44. D. McGloin and K. Dholakia, "Bessel beams: diffraction in a new light," Cont. Phys. **46**, 15–28 (2005).
45. A. Stockham and J. G. Smith, "Optical design for generating Bessel beams for micromanipulation," Proc. SPIE **63211**, 63261D (2006).
46. P. Zhang, Y. Hu, D. Cannan, A. Salandrino, T. Li, R. Morandotti, X. Zhang, and Z. Chen, "Generation of linear and nonlinear nonparaxial accelerating beams," Opt. Lett. **37**, 2820–2822 (2012).
47. P. Zhang, Y. Hu, T. Li, D. Cannan, X. Yin, R. Morandotti, Z. Chen, and X. Zhang, "Nonparaxial Mathieu and Weber accelerating beams," Phys. Rev. Lett. **109**, 193901 (2012).
48. F. O. Fahrbach and A. Rohrbach, "Propagation stability of self-reconstructing Bessel beams enables contrast-enhanced imaging in thick media," Nat. Commun. **3**, 632 (2012).
49. J. P. Rice, J. E. Neira, M. Kehoe, and R. Swanson, "DMD diffraction measurements to support design of projectors for test and evaluation of multispectral and hyperspectral imaging sensors," Proc. SPIE **7210**, 72100D (2009).
50. X. Chen, B. Yan, F. Song, Y. Wang, F. Xiao, and K. Alameh, "Diffraction of digital micromirror device gratings and its effect on properties of tunable fiber lasers," Appl. Opt. **51**, 7214–7220 (2012).
51. H. Ryoo, D. W. Kang, and J. W. Hahn, "Analysis of the effective reflectance of digital micromirror devices and process parameters for maskless photolithography," Microelectron. Eng. **88**, 235–239 (2011).
52. J. Zhao, P. Zhang, D. Deng, J. Liu, Y. Gao, I. D. Chremmos, N. K. Efremidis, D. N. Christodoulides, and Z. Chen, "Observation of self-accelerating Bessel-like optical beams along arbitrary trajectories," Opt. Lett. **38**, 498–500 (2013).
53. Q. Zhan, "Cylindrical vector beams: from mathematical concepts to applications," Adv. Opt. Photon. **1**, 1–57 (2009).